Journal of Physics Research and Education, Volume 3, March 2026

Probing Nuclear Deformation and Clustered Structure Through Photon Anisotropic Flow in Relativistic Nuclear Collisions

Rupa Chatterjee*

Variable Energy Cyclotron Centre, 1/AF, Bidhan Nagar, Kolkata-700064, India and
Homi Bhabha National Institute, Training School Complex, Anushaktinagar, Mumbai 400094, India

Relativistic collisions of nuclei with different intrinsic structures provide a unique opportunity to study how nuclear geometry and deformation influence the initial conditions and the subsequent evolution of the hot and dense quark gluon plasma created in such collisions. Observables measured in collisions involving deformed uranium nuclei, clustered light nuclei such as carbon and oxygen, and isobaric systems such as ruthenium and zirconium offer complementary insights into the properties of the initial state, extending the information obtained from collisions of nearly spherical nuclei. The deformation and possible cluster substructures in the colliding nuclei are expected to generate distinct initial geometric features in the overlap region, while isobaric collisions enable the study of nuclear structure effects in systems with nearly identical mass numbers. These differences influence the initial spatial anisotropies, which subsequently translate into final state momentum anisotropies of the produced particles. The production and anisotropic flow v_n of thermal photons serve as an effective probe of early stage dynamics in relativistic nuclear collisions. A systematic analysis of photon v_n in different collision systems can therefore help identify the effects of nuclear deformation and clustering in the initial state.

I. INTRODUCTION

Relativistic heavy ion collisions lead to the formation of a hot and dense quark–gluon plasma (QGP), a phase of matter in which quarks and gluons are deconfined and exist in local thermal equilibrium [1–5]. It is well established that, a few microseconds after the Big Bang, our present day Universe was in the quark–gluon plasma phase [6]. The core of neutron stars is also believed to contain matter under extreme conditions, where a QGP phase may exist [7]. The hot and dense QGP produced in relativistic heavy-ion collisions is transient in nature, with a lifetime of only a few fm/c. This extremely short existence makes it challenging to extract detailed information about the properties and dynamics of this hot and dense state. Information about the quark gluon plasma and its evolution is extracted from various final state observables measured in experiments [8, 9]. The Relativistic Heavy Ion Collider (RHIC) at Brookhaven National Laboratory first provided strong evidence for the formation of the QGP in Au+Au collisions at 200A GeV energy [10–12]. Subsequently, experimental data from Pb+Pb collisions at the Large Hadron Collider (LHC) at CERN have yielded more detailed insights into the properties and behavior of strongly interacting matter under extreme conditions.

* rupa@vecc.gov.in

Anisotropic flow of charged particles and jet quenching arising from the energy loss of high energy partons (quarks and gluons) traversing the medium are two powerful signatures of quark gluon plasma formation in relativistic heavy ion collisions [13–20]. In addition, strangeness enhancement, heavy quark and quarkonia suppression, electromagnetic probes, and several other observables provide valuable information about the properties of QGP [21]. In relativistic nuclear collisions, the two Lorentz contracted nuclei travel along the beam direction at velocities close to the speed of light and deposit enormous amount of energy in the collision region. Shortly after the collision, the deconfined quarks and gluons interact among themselves to form a strongly interacting medium, which subsequently expands and cools down. After some time, the medium constituents are assumed to stop interacting with one another, leading to a kinetic freeze-out, and the produced particles reach the detector.

Central collisions of two nuclei at relativistic energies are expected to generate the maximum energy density and temperature creating a low baryon density quark gluon plasma matter. In contrast, non-central collisions provide important geometry driven information that cannot be accessed in central collisions [21]. A variety of collision systems, such as Au+Au, Cu+Cu, U+U, Ru+Ru and Zr+Zr have been studied at different beam energies at the Relativistic Heavy Ion Collider. At the Large Hadron Collider, collision systems such as Pb+Pb, Xe+Xe and O+O are explored at even higher energies to investigate the properties of the produced medium through various final state observables. While symmetric collisions of nearly spherical nuclei provide essential information about the properties of the fireball, collisions involving deformed nuclei (such as U+U and Xe+Xe) offer additional and complementary insights that cannot be obtained from spherical systems alone. Recent studies have shown that small systems, like p+p, p+A, d+A and He+Au collisions can also produce QGP due to the compact size and very high energy density formed in these collisions [22–24]. Most of the particles produced in relativistic nuclear collisions are hadrons, with pions comprising the largest number due to their relatively small masses. These hadrons are primarily emitted during the later stages of the evolution and reach the detector after being released from the freeze-out surface. Electromagnetic probes like photons and dileptons are produced throughout the evolution of the expanding fireball [25–29].

A. Anisotropic flow in relativistic nuclear collisions

Anisotropic flow is considered as one of the most prominent observables produced in relativistic nuclear collisions, which provides information about the collective behavior of the produced medium [15, 30, 31]. The initial spatial anisotropy in the overlap region of two colliding nuclei generates anisotropic pressure gradients, which subsequently lead to an anisotropic momentum distribution of the produced particles. This anisotropy is quantified through the Fourier coefficients of the invariant transverse momentum distribution of the produced particles.

$$\frac{dN}{d^2p_T dy} = \frac{1}{2\pi}\frac{dN}{p_T dp_T dy}[1 + 2\sum_{n=1}^{\infty} v_n(p_T)\cos n(\phi - \psi_n)]\,. \tag{1}$$

Here p_T is the particle transverse momentum, y denotes the rapidity and ϕ represents the azimuthal angle of the emitted particles. The event plane angle for the nth flow coefficient is denoted by ψ_n. The event plane angle provides a quantitative measure of the orientation of the anisotropy in each event. The anisotropic flow coefficients v_n from experimental analysis can be compared with

theoretical model calculations to probe key properties of the quark–gluon plasma, such as its shear viscosity, formation time, equation of state, and many more [8, 15].

Anisotropic flow coefficients are commonly studied as functions of transverse momentum, impact parameter (or collision centrality), rapidity, and other kinematic variables. Among the various v_n coefficients, the second harmonic, which originates from the elliptic shape of the overlap region, is typically the largest and is known as the elliptic flow parameter v_2. The third harmonic arises mainly from event-by-event fluctuations in the initial geometry and is referred to as the triangular flow parameter v_3. The directed flow coefficient v_1, particularly in asymmetric collision systems, has also gained considerable attention in recent studies. Higher-order flow coefficients are generally smaller in magnitude compared to v_2 and v_3.

The anisotropic flow of charged particles produced in relativistic heavy-ion collisions is well described by relativistic hydrodynamic models with appropriate initial conditions at both RHIC and LHC energies [8]. In contrast, the anisotropic flow of photons exhibits a different behavior from that of hadrons and remains inadequately described by existing theoretical models [32–35]. This discrepancy between theoretical predictions and experimental observations is commonly referred to as the direct photon puzzle [36].

B. Photon anisotropic flow

Photons produced in relativistic nuclear collisions are regarded as one of the promising probes to study the initial state and the evolution of the fireball. Photons, both real as well as virtual (dileptons), are emitted from the entire space-time evolution and suffer negligible final state interactions. Depending on their origin, photons can be classified into different components such as prompt, thermal, pre-equilibrium and decay photons. The experimentally measured photon spectrum contains a huge background of decay photons which are produced after the freeze-out. Significant progress has been achieved in photon analysis techniques that allow efficient subtraction of the decay photon (mostly originating from the 2γ decay of π^0 and η) contributions from the measured spectrum [29, 37].

Prompt photons are produced in the initial hard scattering among the partons soon after the collisions [38–40]. The next to leading order perturbative QCD calculations for prompt photons matches with experimental data from p+p collisions well both at RHIC and at the LHC energies. These photons do not contribute to the photon anisotropic flow directly as they are emitted before the onset of collectivity of the medium. Thermal photons are emitted from both the QGP phase and the hot hadronic matter phase [41–43]. In the QGP phase, the dominant processes for thermal photon production are quark-gluon Compton scattering and quark anti-quark annihilation. In the hadronic phase, interactions involving π and ρ mesons contribute significantly to the production of thermal photons. The total thermal emission is estimated by integrating the emission rates over the space-time four-volume

$$E\frac{dN}{d^3p} = \int d^4x\, R\left(E^*(x), T(x)\right), \tag{2}$$

where E and p denote the photon energy and momentum, respectively, and $T(x)$ is the local temperature. $E^*(x) = p^\mu u_\mu(x)$ in the boosted frame, where p^μ is the photon four-momentum and u_μ is the local four-velocity of the flow field. Standard rates of photon production from the strongly interacting and dynamically evolving medium are used to estimate the thermal spectra [44–46].

The competing contribution of thermal radiation from QGP and hadronic matter gives rise to the photon anisotropic flow and also decides its p_T dependent nature. The thermal photons only contribute directly to the experimentally measured anisotropic flow of photons. Photons produced just before the thermalization of the medium are known as pre-equilibrium photons [47–49]. These are expected to contribute to the experimentally measured spectrum mainly in the higher p_T region. However, their contribution to the photon anisotropic flow is found to be marginal.

II. PHOTON ANISOTROPIC FLOW FROM COLLISIONS OF NON-SPHERICAL NUCLEI

A. Photons from ^{238}U+^{238}U collisions at RHIC

Collisions involving deformed nuclei have attracted significant attention in recent years [50, 51]. Uranium–uranium collisions at 193A GeV at RHIC and xenon–xenon collisions at 5.44A TeV at the LHC have provided valuable insight into the properties of the hot and dense fireball created in these collisions [52–56]. In recent years, collisions of non-spherical isobaric systems such as Zr+Zr and Ru+Ru at 200A GeV at RHIC have been studied to investigate the chiral magnetic effect in relativistic nuclear collisions [57–59]. The production and anisotropic flow of thermal photons from these systems have shown significant potential not only for probing the initial state nuclear deformation but also for providing insights into the direct photon puzzle [60]. Relativistic hydrodynamics is considered to be the most successful framework to explain the evolution of the medium formed in relativistic nuclear collisions and also the experimentally measured spectra and anisotropic flow of charged particles [8].

The initial state in a hydrodynamical model calculation is typically constructed using the Glauber model formalism. For deformed nuclei, a two-parameter Woods–Saxon nuclear density distribution of the following form is employed [8, 61]:

$$\rho_A(r,\theta) = \frac{\rho_0}{1+\exp\left[\frac{r-R(\theta)}{\xi}\right]}, \tag{3}$$

where ρ_0 is the central density, ξ is surface diffuseness parameter and $R(\theta)$ is the radius of the nucleus A. For uranium the radius is expressed as,

$$R(\theta) = R_A\left[1+\beta_2 Y_{20}(\theta)+\beta_4 Y_{40}(\theta)\right] . \tag{4}$$

Here R_A denotes the nuclear radius in the absence of deformation, defined as,

$$R_A = (1.12A^{1/3} - 0.86A^{-1/3}) \text{ fm}. \tag{5}$$

The parameters β_2 and β_4 represent the quadrupole and hexadecapole deformations, respectively. The $Y_{20}(\theta)$ and $Y_{40}(\theta)$ are the spherical harmonics:

$$Y_{20}(\theta) = \sqrt{\frac{5}{16\pi}}\left(3\cos^2\theta - 1\right) \tag{6}$$

$$Y_{40}(\theta) = \sqrt{\frac{9}{256\pi}}\left(35\cos^4\theta - 30\cos^2\theta + 3\right) . \tag{7}$$

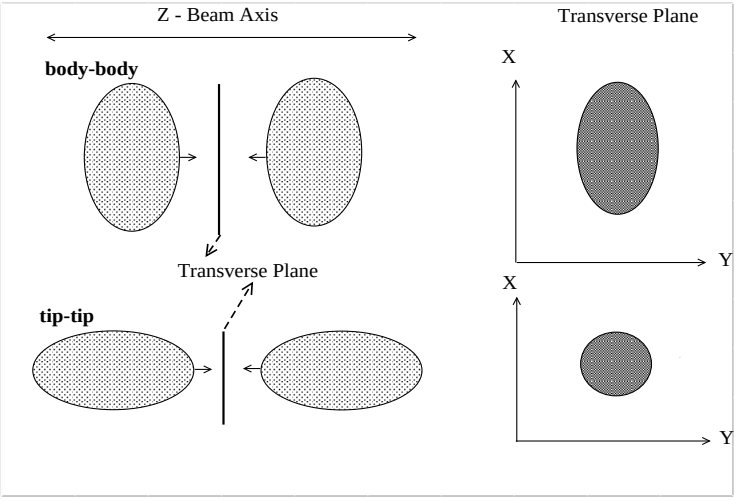

FIG. 1. Schematic representation of the full nuclear overlap for tip–tip and body–body configurations in U+U collisions in the transverse plane [62].

In the Glauber model calculations, the thickness function $T_A(x, y)$ is estimated as a first step, which gives the nucleon density in the transverse plane. In a typical hydrodynamic model calculation, the beam direction is chosen along the z-axis, the impact parameter along the x-axis, and the transverse plane of collisions is the x-y plane. The thickness function is estimated by integrating the nuclear density along the longitudinal (beam) direction:

$$T_A(x, y) = \int dz\, \rho_A(x, y, z), \tag{8}$$

where $\rho_A(x, y, z)$ is the nuclear density distribution (Eq. 3) in the Cartesian coordinate system of the nucleus. For a non-central collision of the nuclei A and B at an impact parameter b, the density of binary nucleon-nucleon collisions, denoted as $n_{\text{coll}}(x, y; b)$ in the transverse plane, is proportional to the product of the two nuclear thickness functions:

$$n_{\text{coll}}(x, y; b) = \sigma_{\text{NN}}\, T_A(x + b/2, y)\, T_B(x - b/2, y), \tag{9}$$

where σ_{NN} denotes the total inelastic nucleon–nucleon cross section at a given beam energy. The total number of binary collisions is obtained as:

$$N_{\text{coll}}(b) = \int\int dx\, dy\, n_{\text{coll}}(x, y; b). \tag{10}$$

The wounded nucleons or participants are those that suffer at least one collision with a nucleon from the other nucleus. The wounded nucleon density $n_{\text{part}}(x, y; b)$ is:

$$\begin{aligned} n_{\text{part}}(x, y; b) = {} & T_A(x + b/2, y)\left[1 - \exp\left(-\sigma_{\text{NN}} T_B(x - b/2, y)\right)\right] \\ & + T_B(x - b/2, y)\left[1 - \exp\left(-\sigma_{\text{NN}} T_A(x + b/2, y)\right)\right]. \end{aligned} \tag{11}$$

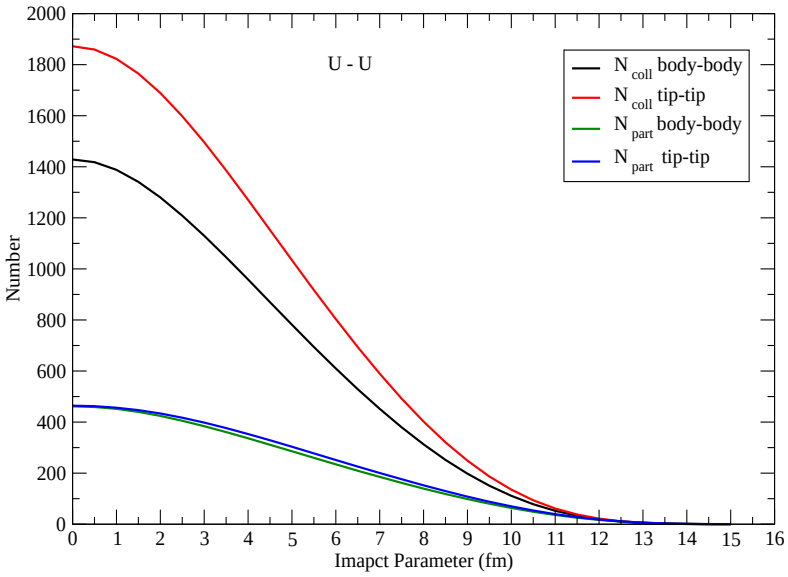

FIG. 2. Number of participants and binary collisions as a function of impact parameter from 193A GeV U+U collisions at RHIC for tip–tip and body–body orientations.

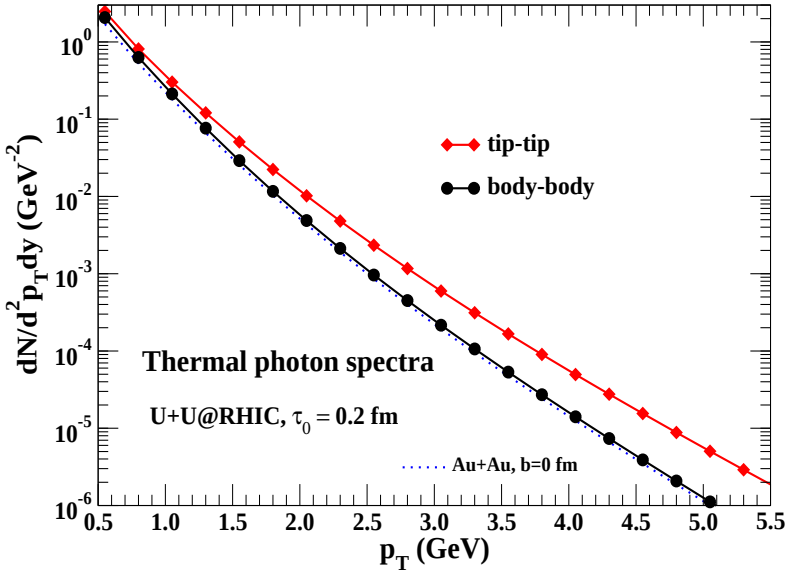

FIG. 3. Thermal photon spectra from tip-tip and body-body U+U collisions at RHIC [62].

The total number of participants in collisions of two nuclei is given by,

$$N_{\text{part}}(b) = \int\int dx\, dy\, n_{\text{part}}(x, y; b). \tag{12}$$

One of the most interesting aspects of collisions involving deformed nuclei is that even in fully

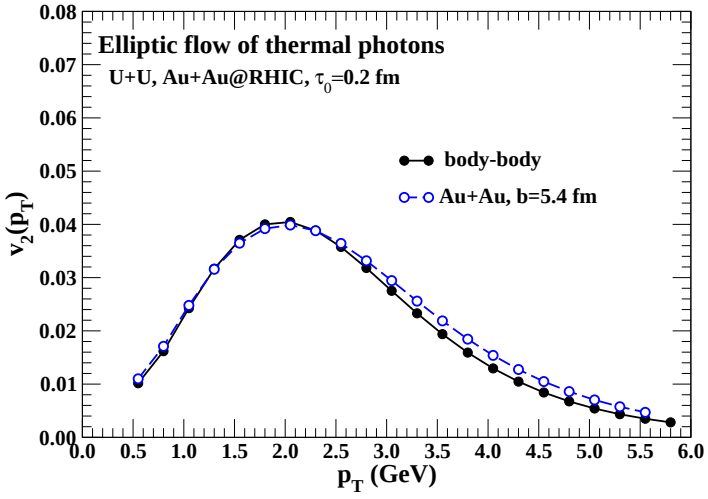

FIG. 4. Elliptic flow of thermal photons from body-body orientation of U+U collisions and mid-central Au+Au collisions at RHIC [62].

overlapping most-central collisions, different orientations of the colliding nuclei can lead to distinct initial geometries and significantly different final state observables. A fully overlapping U+U collision that gives rise to a maximum energy density, charged particle multiplicity, and a circular overlapping region is called the tip-tip orientation [see Fig. 1]. The other fully overlapping orientation that gives rise to minimum energy density and maximum spatial eccentricity is known as the body-body collisions, as shown in Fig. [62]. Glauber model calculations show that, although the number of participants depends only marginally on the collision orientation, the number of binary collisions is about 30% larger for the tip–tip collisions compared to the body–body collisions, as shown in Fig. 2. For ^{238}U the deformation parameters β_2 and β_4 are taken as 0.28 and 0.093, respectively. The σ_{NN} value at 200A GeV is taken to be 42 mb.

A (2+1) dimensional longitudinally boost invariant ideal hydrodynamical model calculation has been used along with state of the art thermal photon rates to calculate the spectra from tip-tip and body-body orientations in U+U collisions at RHIC [62]. The results, along with thermal photon spectra from central Au+Au collisions, are shown in Fig. 3. The thermal production is found to be significantly larger for the tip-tip collisions than for body-body collisions, as the initial temperature distribution is much larger for the former than for the latter. The elliptic flow parameter, on the other hand, is found to be significantly large for the body-body orientation [see Fig. 4] and comparable to the $v_2(p_T)$ for mid-central Au+Au collisions at RHIC. The tip-tip orientation does not give rise to significant photon elliptic flow due to the absence of spatial anisotropy in the initial overlapping region. One can expect only a very small $v_2(p_T)$ from the tip-tip collision due to initial state fluctuations.

It has been shown that the spectator energy deposited in the zero-degree calorimeter can be used experimentally to select the most central events. In addition, the anti-correlation between particle multiplicity and anisotropic flow can, in principle, help distinguish between the tip-tip and body-body configurations in most central U+U collisions. Therefore, an experimental determination of photon anisotropic flow in U+U collisions could provide further insight into the direct photon puzzle by comparing with the direct photon data from Au+Au collisions and help constrain the properties of the initial state created in such collisions [62].

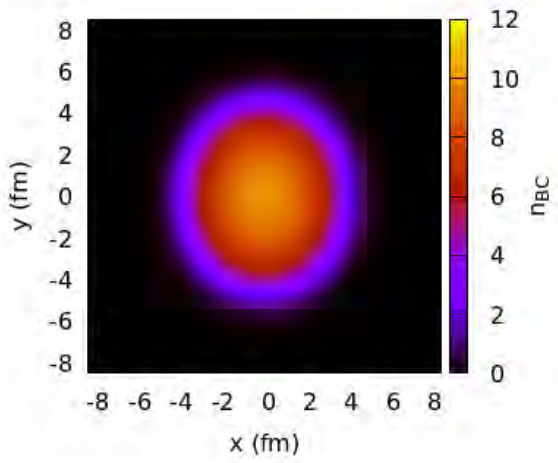

FIG. 5. Density of binary collisions $n_{\rm BC}$ in the transverse plane at impact parameter b = 0 fm for Ru+Ru body-body collision at 200A GeV at RHIC.

B. Anisotropic flow of thermal photons from isobaric collisions at RHIC

Isobars are nuclei that have the same mass number A and different atomic (charge) numbers Z. Relativistic collisions of isobaric systems provide a unique opportunity to study the influence of nuclear structure and charge differences on various observables for nearly identical systems [57]. The isobaric collisions of ^{96}Ru+^{96}Ru ($A = 96$, $Z = 44$) and ^{96}Zr+^{96}Zr ($A = 96$, $Z = 40$) were carried out recently at $\sqrt{s_{NN}} = 200$ GeV at RHIC. The ^{96}Ru nucleus is believed to exhibit a prolate deformation, whereas ^{96}Zr is expected to exhibit octupole deformation, despite both nuclei having the same mass number [63–65]. As a result, these systems provide an important testing ground to study the effects of nuclear deformation and properties of the initial state in relativistic nuclear collisions. A hydrodynamic model calculation has been carried out to study the initial state, its evolution, thermal photon production, and anisotropic flow of photons from different orientations of Ru+Ru and Zr+Zr collisions [60]. The initial entropy density is considered to be proportional to the final charged particle multiplicity. Since the value of charged particle multiplicity for the isobaric set is not known precisely, we use the parametrized relation [66]:

$$\frac{dN_{\rm ch}}{d\eta} = \frac{N_{\rm WN}}{2}\left[0.78\ln\left(\sqrt{s_{\rm NN}}\right) - 0.4\right]. \tag{13}$$

The nuclear radius in the density distribution in the initial state Glauber model calculation for Ru is taken as,

$$R(\theta,\phi) = R_A\left[1 + \beta_2 Y_{20}(\theta,\phi)\right]. \tag{14}$$

For the Zr it is taken as,

$$R(\theta,\phi) = R_A\left[1 + \beta_2 Y_{20}(\theta,\phi) + \beta_3 Y_{30}(\theta,\phi)\right]. \tag{15}$$

The parameters used for the isobaric systems are listed in Table I. Due to the deformed nuclear

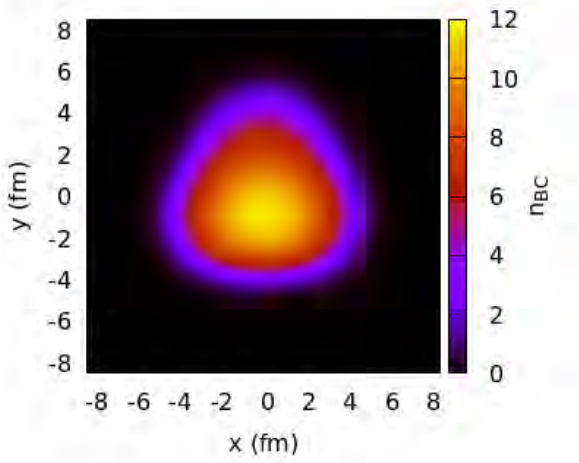

FIG. 6. Density of binary collisions $n_{\rm BC}$ in the transverse plane at impact parameter b = 0 fm for Zr+Zr body-body collision at 200A GeV at RHIC.

structure of these nuclei, the hydrodynamic evolution of the medium produced in these collisions is found to be slightly different for the two systems. In the most central body-body configuration, Zr+Zr collisions generate a relatively large initial triangular eccentricity, whereas Ru+Ru collisions lead to a larger elliptic eccentricity. The distributions of the number of binary collisions in the transverse plane for the body-body collisions of Ru+Ru and Zr+Zr at $\sqrt{s_{NN}} = 200$ GeV at RHIC are shown in Fig. 5 and Fog. 6, respectively. The initial spatial anisotropy arising from the nuclear structure leads to significant anisotropic flow of photons in the most central events.

It has been shown that Zr+Zr collisions produce a relatively large triangular flow $v_3(p_T)$ of photons, whereas Ru+Ru collisions result in a larger elliptic flow of thermal photons [see [60] for details]. The magnitude of the triangular flow is found to be significantly larger than the elliptic flow parameter in this set of isobaric collisions. Therefore, the ratio v_2/v_3 of photons together with the individual anisotropic flow coefficients can serve as a useful probe of the underlying nuclear structure and the properties of hot and dense QGP matter produced in these collisions.

Nucleus	A	R_A (fm)	ξ (fm)	β_2	β_3
Ruthenium (Ru)	96	5.09	0.46	0.162	0
Zirconium (Zr)	96	5.02	0.52	0.06	0.20

TABLE I. Nuclear parameters and deformation parameters for different nuclei [63].

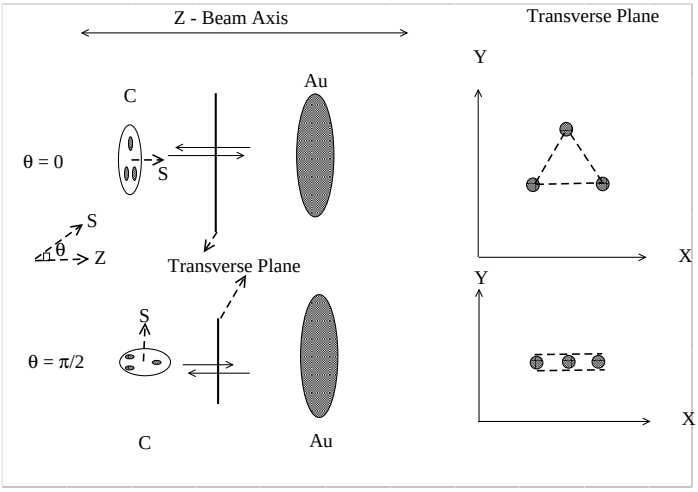

FIG. 7. Schematic of two different orientations of α clustered carbon colliding with gold nuclei [75].

III. COLLISION OF ALPHA CLUSTERED LIGHT NUCLEI

The existence of α-cluster configurations in light nuclei, such as ^{12}C and ^{16}O, constitutes a key aspect of low-energy nuclear structure physics [67, 68]. These substructures are believed to play an important role in the stability and structural properties of these nuclei. Recent theoretical and phenomenological studies indicate that α clustered structures in light nuclei can be probed in relativistic nuclear collisions by analyzing the final state observables which carry information about the initial geometric structure of the colliding nuclei [69–73]. One can estimate that the passage time of two Lorentz contracted nuclei in relativistic nuclear collisions is significantly shorter than the characteristic timescale of slower nuclear reactions. Consequently, in the collisions involving α clustered light nuclei, the initial geometric configuration is expected to remain effectively frozen in the early stages of the interaction.

The ^{12}C nucleus is commonly modeled as three α clusters located at the vertices of an equilateral triangle, whereas the ^{16}O nucleus is often described by a four α cluster configuration. The nucleon distribution in clustered ^{12}C is constrained such that the one-body radial density distribution reproduces the results of the BEC model [74]. The nucleon distribution within each α cluster of ^{12}C is assumed to follow a Gaussian form:

$$f_i(\vec{r}) = \mathcal{A} \exp\left(-\frac{3}{2}(\vec{r} - \vec{c_i})^2/r_\alpha^2\right), \tag{16}$$

where the center of the i^{th} cluster is denoted by $\vec{c_i}$, and the cluster radius is represented by r_α. The side length of the equilateral triangle configuration is taken to be 3.05 fm, while r_α is chosen as 0.96 fm. For details, see Ref. [75] and the references therein. The unclustered configuration of the carbon nucleus corresponds to the mean-field state, where the nucleon distribution is assumed to be isotropic. For the unclustered carbon nucleus, a two-parameter Woods–Saxon density distribution is employed with parameters tuned to reproduce the same root-mean-square radius (~ 2.26 fm) as in the clustered configuration. The initial density distribution of the gold nucleus is also described using the standard two-parameter Woods–Saxon nuclear density profile.

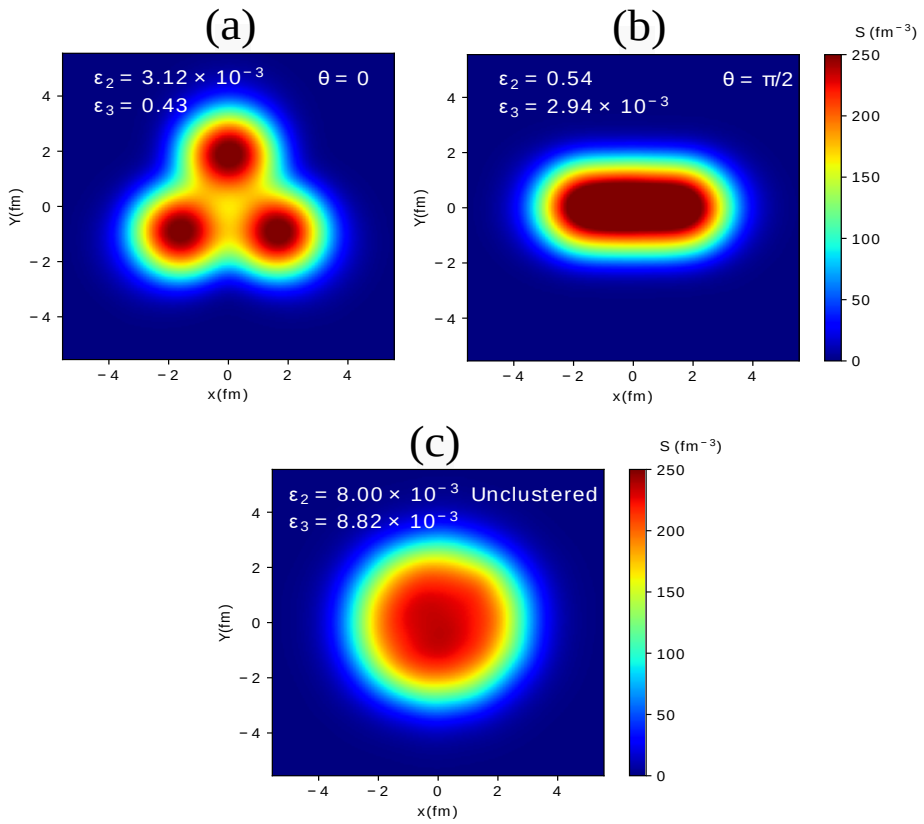

FIG. 8. Initial entropy density distribution on the transverse plane in clustered C+Au collisions for two different orientations (upper panels) and for most central unclustered C+Au collisions (lower panel) at 200A GeV at RHIC [75].

Figure 7 shows a schematic diagram of the collision of alpha-clustered carbon with gold nuclei for two different orientations of the clustered carbon. Depending on the orientation of the clustered carbon, the collision geometry varies significantly as the nuclear distribution of the gold nuclei is random, and it acts as a wall to the incoming carbon nucleus. Thus, when the symmetry axis of the carbon nucleus is aligned along the z-axis, it results in a large triangular eccentricity ϵ_3 (see Fig. 8 (a)). In contrast, when the symmetry axis is oriented perpendicular to the beam direction, it leads to a large spatial ellipticity ϵ_2 as shown in Fig. 8 (b). The central collision of unclustered or uniform carbon with a gold nucleus results in a uniform distribution of initial energy or entropy density on the transverse plane, as shown in Fig. 8 (c).

A realistic simulation considering an event-by-event hydrodynamical evolution has shown that the event averaged initial eccentricities of cluster C+Au collision show a completely different nature than the results obtained from the unclustered C+Au collisions at 200A GeV at RHIC [76]. The initial spatial eccentricities ϵ_n are obtained using the relation [77]:

$$\varepsilon_n = \frac{\sqrt{\langle r^2 \cos(n\phi)\rangle^2 + \langle r^2 \sin(n\phi)\rangle^2}}{\langle r^2 \rangle} \,. \tag{17}$$

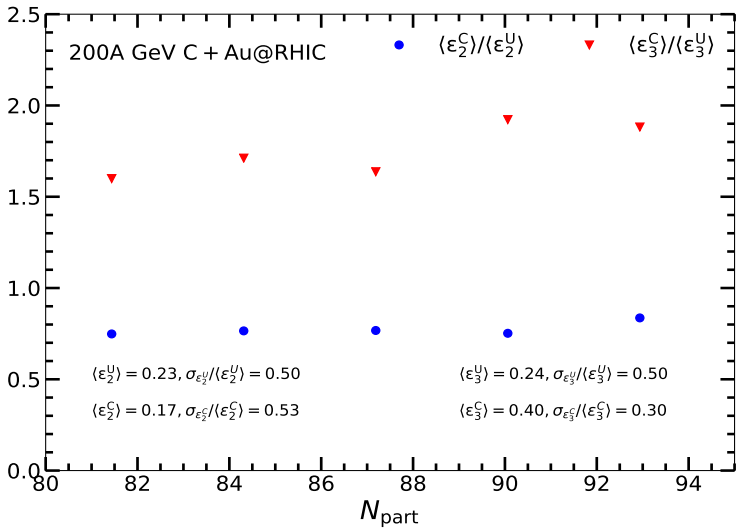

FIG. 9. Ratio of initial spatial eccentricities (ϵ_2 and ϵ_3) from clustered and unclustered C+Au collisions at RHIC as a function of collision centrality [76].

As shown in Fig. 9, the initial triangular eccentricity ε_3 is significantly larger for the clustered case compared to the unclustered case in the most central collisions. In contrast, the initial ellipticity ε_2 does not differ appreciably between the clustered and unclustered configurations, resulting in a ratio that remains close to unity.

In the Monte Carlo Glauber framework used in event-by-event hydrodynamical model simulation, two nucleons from different nuclei are assumed to collide when the transverse distance between the colliding nucleons d satisfies the criterion: $d^2 < \frac{\sigma_{\rm NN}}{\pi}$. The initial energy ($\epsilon(x,y)$) or entropy density ($s(x,y)$) distribution is assumed to be of the form [76]:

$$\epsilon(x,y)\, or\, s(x,y) = K \sum_{i,j=1}^{N_{\rm part},N_{\rm coll}} [\,\nu\, n_{\rm coll}(x_i,y_i) F_i(x,y) + (1-\nu)\, n_{\rm part}(x_j,y_j)\; F_j(x,y)]. \quad (18)$$

The value of the constant factor ν is taken as 0.145, and K is a normalization factor that decides the total multiplicity of an event. A normalized Gaussian distribution function $F_{i,j}(x,y)$ is centered about the i^{th} participant or j^{th} collision source is like:

$$F_{i,j}(x,y) = \frac{1}{2\pi\sigma^2}\, e^{-\frac{(x-x_{i,j})^2+(y-y_{i,j})^2}{2\sigma^2}}. \quad (19)$$

The Gaussian smearing width σ is taken as 0.4 fm. For thermal photon calculation, the initial formation time of the plasma at RHIC is taken as 0.17 fm/c and a lattice based equation of state is considered with freeze-out temperature of 160 MeV [78]. The thermal photon spectra averaged over a sufficiently large number of events from clustered and unclustered C+Au collisions at RHIC

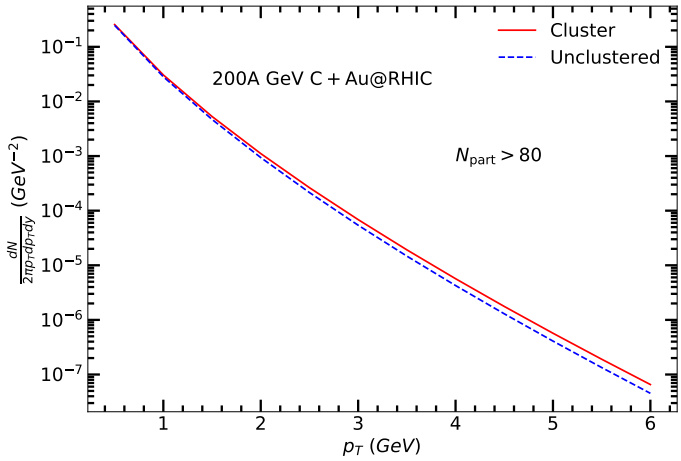

FIG. 10. Thermal photons spectra from clustered and unclustered most central C+Au collisions at 200A GeV RHIC [76].

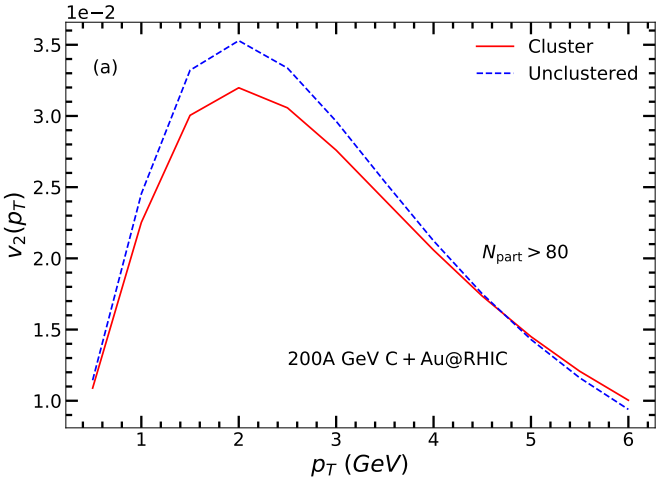

FIG. 11. Elliptic flow parameter $v_2(p_T)$ of thermal photons from clustered and unclustered C+Au collisions at 200A GeV at RHIC. [76]

are shown in Fig. 10. The figure shows that the photon spectra alone can not differentiate between the cluster and unclustered state of the colliding light nuclei. On the other hand, the anisotropic flow exhibits significant qualitative and quantitative differences between the clustered and unclustered configurations in these collisions. The elliptic and triangular flow coefficients of thermal photons for the two configurations are shown in Fig. 11 and Fig. 12, respectively.

The p_T-dependent elliptic flow of thermal photons from the collisions of clustered and unclustered carbon is found to be close to each other. The $v_2(p_T)$ from unclustered collisions is found

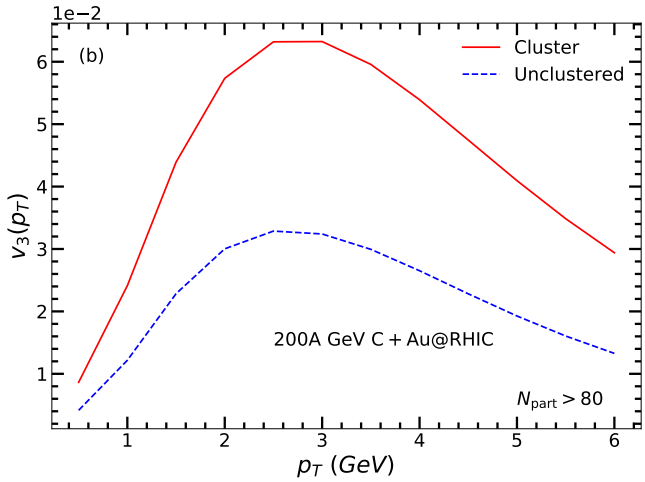

FIG. 12. Triangular flow parameter $v_3(p_T)$ of thermal photons from clustered and unclustered C+Au collisions at 200A GeV at RHIC [76].

to be a little larger than the clustered case. This can be due to the relatively smaller ε_2 for the clustered C+Au collisions. The triangular flow, on the other hand, is found to be significantly larger for the clustered C+Au collisions than for the unclustered case. The magnitude of $v_3(p_T)$ is also found to be larger than $v_2(p_T)$ from both clustered and unclustered collisions. This nature of the anisotropic flow is unique, as for spherical nuclei, the triangular flow is found to be always smaller than the elliptic flow parameter. Thus, the experimental determination of the anisotropic flow of photons from such collisions can be useful in the study of the initial clustered structure in light nuclei.

It is to be noted that prompt photons produced from initial hard scatterings do not contribute to the elliptic flow of photons directly. However, they dilute the flow parameter in the larger p_T region by adding an extra weight factor. The thermal photon anisotropic flow is modified due to the prompt contribution as,

$$v_n(p_T) = \frac{dN^{\rm th}(p_T) \times v_2^{\rm th}(p_T)}{dN^{\rm th}(p_T) + dN^{\rm pr}(p_T)}, \tag{20}$$

where $dN^{\rm th}(p_T)$ and $dN^{\rm pr}(p_T)$ are the thermal and prompt yield at p_T and $v_2^{\rm th}(p_T)$ is the corresponding thermal photon v_2. The contribution of prompt photons to the experimentally measured direct photon spectrum is substantial above $p_T = 3$ GeV/c. Thus, the inclusion of prompt photons affect the anisotropic flow mostly above 3 GeV/c. Minimizing the contribution of the prompt photons we have shown in a recent study that the ratio of photon anisotropic flow parameters can be a potential probe in this regard [79]. The ratio of photon anisotropic flow parameters from clustered and unclustered C+Au collisions is shown in Fig. 13. For cluster collisions, the ratio is less than 1 for $p_T > 1$ GeV/c. However, for the unclustered C+Au collisions, the ratio is much larger than 1 for $p_T < 3$ GeV/c. This difference between the ratio results for the two cases can be a potential probe to study the initial state clustered structure in light nuclei.

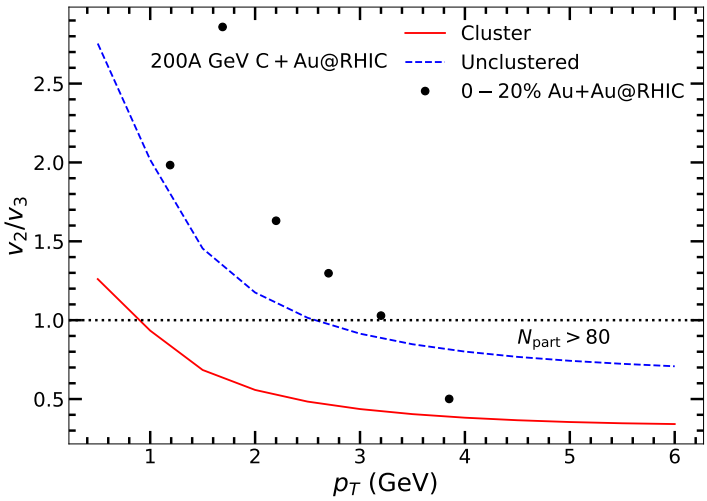

FIG. 13. The ratio of photon anisotropic flow parameters from clustered and unclustered C+Au collisions at 200A GeV at RHIC [76].

A. Anisotropic flow from clustered O+O collisions at LHC

The recent experimental program involving O+O collisions at $\sqrt{s_{NN}} = 7$ TeV at the LHC provides a new opportunity to investigate the possible clustered structure in light nuclei. The ^{16}O nucleus is predicted to exhibit a α clustered configuration in which four α particles are located at the vertices of a tetrahedron. This geometric arrangement leads to spatial correlations among the nucleons that can influence the initial spatial anisotropy of the collision zone in relativistic nuclear collisions. Consequently, the measurements of final state observables such as anisotropic flow parameters can provide information about the underlying cluster structure of the oxygen nucleus.

A relativistic hydrodynamic simulation with the GLISSANDO initial conditions has been employed to study O+O collisions at 7A TeV for both the clustered and unclustered configurations [80]. The initial spatial eccentricities, as well as the evolution of average transverse flow velocity, average temperature, etc., are studied in detail, and the results show moderate differences in the evolution of thermodynamic parameters between clustered and unclustered O+O collisions. The thermal photon spectra are found to be largely insensitive to the clustered structure of the nucleus. However, the qualitative behavior of the anisotropic flow parameters depends strongly on the presence of clustering in the oxygen nucleus.

IV. SUMMARY AND CONCLUSIONS

In conclusion, relativistic nuclear collisions involving nuclei with intrinsic deformation offer an effective way to investigate the influence of nuclear structure on the initial conditions and the subsequent evolution of the produced medium. These studies complement the information obtained from collisions of nearly spherical nuclei, where the effects of deformation are largely

absent. Relativistic collisions of light nuclei such as oxygen and carbon offer a unique opportunity to explore the possible α-clustered configurations in the nuclear structure. The spatial correlations associated with these clustered arrangements can modify the initial geometry of the overlap region and may be reflected in final state observables, such as the anisotropic flow coefficients.

Measurements of photon anisotropic flow in these systems could therefore serve as sensitive probes of the underlying nuclear structure. Additionally, such studies may also contribute to a better understanding of the longstanding direct photon puzzle in relativistic heavy-ion collisions by providing additional constraints on the early time dynamics and photon production mechanisms.

Acknowledgments : The author would like to thank Pingal Dasgupta and Amit Paul for their valuable suggestions and helpful discussions.

[1] J. W. Harris and B. Müller, Ann. Rev. Nucl. Part. Sci. **46**, 71 (1996).
[2] E. Shuryak, Rev. Mod. Phys. **89**, 035001 (2017).
[3] K. Yagi, T. Hatsuda, and Y. Miake, Camb. Monogr. Part. Phys. Nucl. Phys. Cosmol. **23**, 1 (2005).
[4] E. V. Shuryak, Phys. Rept. **61**, 71 (1980).
[5] M. Gyulassy and L. McLerran, Nucl. Phys. A **750**, 30 (2005).
[6] U. W. Heinz, J. Phys. Conf. Ser. **455**, 012044 (2013).
[7] J. C. Collins and M. J. Perry, Phys. Rev. Lett. **34**, 1353 (1975).
[8] P. F. Kolb and U. W. Heinz, arXiv:nucl-th/0305084.
[9] E. V. Shuryak, Phys. Lett. B **78**, 150 (1978).
[10] B. B. Back *et al.*, Nucl. Phys. A **757**, 28 (2005).
[11] J. Adams *et al.*, Nucl. Phys. A **757**, 102 (2005).
[12] K. Adcox *et al.*, Nucl. Phys. A **757**, 184 (2005).
[13] J. Y. Ollitrault, Phys. Rev. D **46**, 229 (1992).
[14] S. A. Voloshin, A. M. Poskanzer, and R. Snellings, arXiv:0809.2949.
[15] U. Heinz and R. Snellings, Ann. Rev. Nucl. Part. Sci. **63**, 123 (2013).
[16] C. Gale, S. Jeon, and B. Schenke, Int. J. Mod. Phys. A **28**, 1340011 (2013).
[17] M. Gyulassy *et al.*, arXiv:nucl-th/0302077.
[18] A. Majumder and M. Van Leeuwen, Prog. Part. Nucl. Phys. **66**, 41 (2011).
[19] G. Y. Qin and X. N. Wang, Int. J. Mod. Phys. E **24**, 1530014 (2015).
[20] K. M. Burke *et al.*, Phys. Rev. C **90**, 014909 (2014).
[21] R. S. Bhalerao, arXiv:1404.3294.
[22] C. Aidala *et al.*, Nat. Phys. **15**, 214 (2019).
[23] G. Aad *et al.*, Phys. Rev. Lett. **116**, 172301 (2016).
[24] S. Chatrchyan *et al.*, Phys. Lett. B **718**, 795 (2013).
[25] E. L. Feinberg, Nuovo Cim. A **34**, 391 (1976).
[26] L. D. McLerran and T. Toimela, Phys. Rev. D **31**, 545 (1985).
[27] D. K. Srivastava, J. Phys. G **35**, 104026 (2008).
[28] G. Vujanovic *et al.*, Nucl. Phys. A **932**, 230 (2014).
[29] G. David, Rept. Prog. Phys. **83**, 046301 (2020).
[30] C. Adler *et al.*, Phys. Rev. Lett. **87**, 182301 (2001).
[31] S. S. Adler *et al.*, Phys. Rev. Lett. **91**, 182301 (2003).

[32] R. Chatterjee *et al.*, Phys. Rev. Lett. **96**, 202302 (2006).
[33] C. Gale *et al.*, Phys. Rev. Lett. **114**, 072301 (2015).
[34] R. Chatterjee *et al.*, Phys. Rev. C **88**, 034901 (2013).
[35] A. Monnai, Phys. Rev. C **90**, 021901 (2014).
[36] R. Chatterjee and P. Dasgupta, Physics **6**, 674 (2014).
[37] R. Chatterjee *et al.*, Lect. Notes Phys. **785**, 219 (2010).
[38] P. Aurenche *et al.*, Phys. Rev. D **73**, 094007 (2006).
[39] P. Aurenche *et al.*, Eur. Phys. J. C **9**, 107 (1999).
[40] L. E. Gordon and W. Vogelsang, Phys. Rev. D **50**, 1901 (1994).
[41] J. I. Kapusta, P. Lichard, and D. Seibert, Phys. Rev. D **44**, 2774 (1991).
[42] R. Baier *et al.*, Z. Phys. C **53**, 433 (1992).
[43] D. K. Srivastava, Phys. Rev. C **64**, 054902 (2001).
[44] P. B. Arnold, G. D. Moore, and L. G. Yaffe, JHEP **12**, 009 (2001).
[45] J. Ghiglieri *et al.*, JHEP **05**, 010 (2013).
[46] S. Turbide, R. Rapp, and C. Gale, Phys. Rev. C **69**, 014903 (2004).
[47] C. Gale *et al.*, Phys. Rev. C **105**, 014909 (2022).
[48] O. Garcia-Montero *et al.*, JHEP **03**, 053 (2024).
[49] A. Monnai, J. Phys. G **47**, 075105 (2020).
[50] U. W. Heinz and A. Kuhlman, Phys. Rev. Lett. **94**, 132301 (2005).
[51] A. J. Kuhlman and U. W. Heinz, Phys. Rev. C **72**, 037901 (2005).
[52] L. Adamczyk *et al.*, Phys. Rev. Lett. **115**, 222301 (2015).
[53] L. Adamczyk *et al.*, Phys. Rev. C **93**, 014907 (2016).
[54] S. Acharya *et al.*, Phys. Lett. B **788**, 166 (2019).
[55] A. M. Sirunyan *et al.*, JHEP **10**, 138 (2018).
[56] M. Aaboud *et al.*, Phys. Lett. B **789**, 444 (2019).
[57] M. S. Abdallah *et al.*, Phys. Rev. C **105**, 014901 (2022).
[58] J. Hammelmann *et al.*, Phys. Rev. C **101**, 061901(R) (2020).
[59] G. Giacalone, J. Jia, and V. Somà, Phys. Rev. C **104**, 041903 (2021).
[60] A. Paul and R. Chatterjee, arXiv:2512.03675.
[61] M. L. Miller *et al.*, Ann. Rev. Nucl. Part. Sci. **57**, 205 (2007).
[62] P. Dasgupta *et al.*, Phys. Rev. C **95**, 064907 (2017).
[63] C. Zhang, S. Bhatta, and J. Jia, Phys. Rev. C **106**, 031901 (2022).
[64] G. Nijs and W. van der Schee, SciPost Phys. **15**, 041 (2023).
[65] J. Jia *et al.*, Nucl. Sci. Tech. **35**, 220 (2024).
[66] B. Alver *et al.*, Phys. Rev. C **83**, 024913 (2011).
[67] G. Gamow, Oxford (1931).
[68] F. Hoyle, Astrophys. J. Suppl. **1**, 121 (1954).
[69] R. Bijker and F. Iachello, Phys. Rev. Lett. **112**, 152501 (2014).
[70] D. Dell'Aquila *et al.*, Phys. Rev. Lett. **119**, 132501 (2017).
[71] W. Broniowski and E. Ruiz Arriola, Phys. Rev. Lett. **112**, 112501 (2014).
[72] P. Bozek *et al.*, Phys. Rev. C **90**, 064902 (2014).
[73] S. Zhang *et al.*, Phys. Rev. C **95**, 064904 (2017).
[74] Y. Funaki *et al.*, Eur. Phys. J. A **28**, 259 (2006).
[75] P. Dasgupta *et al.*, Eur. Phys. J. A **57**, 134 (2021).
[76] P. Dasgupta, R. Chatterjee, and G.-L. Ma, Phys. Rev. C **107**, 064904 (2023).

[77] B. Alver and G. Roland, Phys. Rev. C **81**, 054905 (2010).
[78] R. Chatterjee *et al.*, Phys. Rev. C **85**, 064910 (2012).
[79] R. Chatterjee and P. Dasgupta, Phys. Rev. C **104**, 064907 (2021).
[80] S. Thakur *et al.*, arXiv:2509.20954.